

Journal of Innovative Optical Health Sciences
Vol. 11, No. 2 (2017) 1850008 (8 pages)
© The Author(s)
DOI: 10.1142/S1793545818500086



Co-registered photoacoustic and ultrasound imaging for tongue cancer detection

Heng Guo*, Weizhi Qi*, Ming He*, Jian Rong^{*,†} and Lei Xi^{*,†,‡}

**School of Physical Electronics, University of Electronic
Science and Technology of China
Chengdu, Sichuan, P. R. China*

*†Center for Information in Biomedicine, University of
Electronic Science and Technology of China
Sichuan, P. R. China*

‡xilei1985@uestc.edu.cn

Received 13 July 2017

Accepted 5 September 2017

Published

Tongue cancer is an increasingly common disease with high morbidity. Besides clinical observation, biomedical imaging techniques have been investigated for early detection of tongue cancer. In this paper, we proposed a co-registered dual-modality photoacoustic (PA) and ultrasound imaging technique to simultaneously map the functional and structural information of human tongue, which has the potential to detect and diagnose tongue cancer in early stage. The imaging probe comprises a 20-MHz side-view focused transducer for ultrasound imaging and PA detection, a light path constructed by a multimode optical fiber, and a prism for PA illumination. Phantom experiments were conducted to evaluate the performance of the system including penetration depth, spatial resolution and signal-to-noise ratio. *In vivo* imaging of animal tumor and human tongue was carried out to show the feasibility of the proposed technique to detect tumor lesions in human tongue. The results of phantom and *in vivo* experiments suggest that the proposed technique has the potential to detect the early-stage cancer lesions in human tongue.

Keywords: Tongue cancer; photoacoustic imaging; multimodal imaging.

1. Introduction

Tongue cancer, accompanied with high morbidity, has become one of the common malignant neoplasms in the oral cavity.^{1,2} For most types of cancers,

clinical investigation shows that early intervention can significantly improve the survival rate and prognostic life quality of patients. For instance, 5-year survival rates of stage I and stage IV tongue

[‡]Corresponding author.

This is an Open Access article published by World Scientific Publishing Company. It is distributed under the terms of the Creative Commons Attribution 4.0 (CC-BY) License. Further distribution of this work is permitted, provided the original work is properly cited.

H. Guo et al.

cancers are 82% and 35%, respectively.³ Currently, the most commonly used diagnostic method for tongue cancer is clinical observation followed by pathological analysis.⁴ In clinical observation, physicians inspect the suspicious tissues using naked eyes or some camera-based stomatoscopes. However, clinical observation is subjective, and thus the accuracy highly depends on the clinical experience of physicians. In addition, conventional stomatoscopes are only suitable for superficial lesions.

With the rapid development of new and existing imaging modalities, several clinical and biomedical imaging techniques focusing on detecting and assessing tongue cancer have been reported, such as narrowband imaging (NBI),^{5,6} fluorescence spectroscopy,^{7,8} optical coherence tomography (OCT),^{9,10} computed tomography (CT)^{11,12} and magnetic resonance image (MRI).^{13,14} NBI and fluorescence spectroscopy are able to provide detailed information of the mucosa with high sensitivity and specificity, but limited to superficial tumor lesions. OCT has been used to identify early-stage oral cancer lesions combined with nanoparticles. However, it is only sensitive to morphological changes in the early cancerous stage, and the imaging depth (<3 mm) is still insufficient to detect deep lesions. OCT angiography (OCTA), utilizing flow contrast from red blood cells, is capable of visualizing both structural and functional parameters of vasculatures without coupling medium and with a high spatial resolution. Unfortunately, besides the insufficient penetration depth to cover the entire tongue, the imaging speed is limited by the requirement of repeated scanning in one position. CT scan specifically predict the calcification of the tumor in the early stage. Unfortunately, it suffers from ionizing radiation and low sensitivity to soft tissues. Although MRI has successfully demonstrated to examine tongue tumor lesions in clinics, high cost and low temporal resolution prevent it from routine inspection.

Photoacoustic imaging (PAI) is a hybrid optical imaging technique that combines rich optical contrast and deep penetration with high acoustic resolution.¹⁵ In PAI, wideband acoustic signals generated as a result of thermal expansion are collected and spatially resolved by the acoustic transducer.¹⁶ Nowadays, PAI has been successfully

demonstrated in different research fields such as biology, medicine, and nanotechnology.^{17–20} However, from the fundamental of photoacoustic, PA imaging is only sensitive to optical absorption and can offer limited structural information of high optical absorbing tissues.¹⁶ For most of the normal human tissues with mediate and low optical absorption coefficients such as fat, muscle, nevus, and fiber, the PA signal is too weak to be detected using current acoustic transducers. Ultrasound imaging, based on the different acoustic impedances between tissues, is specialized in providing morphological information of tissues and remains one of the most essential and mature techniques in clinics. Since the ultrasound transducer can detect both PA signals and ultrasound echoes simultaneously, it is feasible to integrate PAI and ultrasound imaging in a single system to obtain both functional and morphological information of tissues. In intravascular and endoscopic research, ultrasound imaging has been extensively combined with different PA imaging modalities such as PA computed tomography, acoustic-resolution PA microscopy and optical-resolution PA microscopy to supplement tissue/organ structures.^{21–23}

During the development of tongue cancer, there exists angiogenesis in the early-stage cancerization of tissues.²⁴ Angiogenesis will result in a large number of newborn blood vessels serving as strong optical absorption contrast to distinguish cancerous tissues from normal tissues for PA imaging. Moreover, the acoustic impedance variance of cancerous lesions provides acoustic contrast for ultrasound imaging. *Oraevesky et al.* demonstrated the feasibility of detecting tumor lesions using PAI and *Fatakdawala et al.* integrated PA microscopy, ultrasound microscopy and fluorescence imaging in a single system to achieve multimodal *in vivo* imaging of oral cancer.^{25,26} Both of the systems are too bulky to be used in a human oral cavity. Hence, in this study, we design and integrate the PA and US imaging into a miniaturized probe to achieve the inspection of potential tongue cancers in human oral cavity. Besides the evaluation of the system performance via phantom experiments and *in vivo* mouse-based tumor model, we successfully visualize both vasculature and tissue structures of the human tongue in three-dimension. This study proves that the proposed dual-modality technique has the potential for detection and diagnosis of the early stage tongue cancer in clinics.

2. Materials and Methods

2.1. System configuration

Figure 1(a) shows the schematic of the proposed system. Laser pulses with a duration of 7 ns and a repetition rate of 20 Hz from an OPO laser (Surelite OPO, Continuum, CA) are split by a thin glass. The reflection pulses are detected by a fast photodiode (818-BB-21, Newport) to monitor the fluctuation of photon energy. The transmission pulses are coupled into a 2 mm optical fiber bundle which is used to deliver the excitation pulses to the tissue surface. Generated PA signals are detected by a focused ultrasonic transducer. A pulse/receiver (5073PR, Olympus) is utilized to drive the transducer to generate acoustic waves for ultrasound imaging and amplify both PA signals and ultrasonic echoes. Both ultrasound and PA signals are

digitalized by a 12 bits DAQ card (NI-5124, National Instruments Corporation, TX) with a sampling rate of 200 Ms/S. A functional generator (DG1022U, Rigol) is employed to provide a delay time between triggers for PAI and ultrasound imaging. We use a wavelength of 750 nm with an optical radiant exposure of 15 mJ/cm^2 which is lower than the American National Standards Institute Safety (ANSI) limit of 22 mJ/cm^2 . No averaging of PA and ultrasound signals is required for all the experiments.

2.2. Imaging interface

As presented in Fig. 1(b), the implemented probe consists of a 20 MHz focused side-view transducer (V3343, Olympus) with an active area of 3 mm in diameter and a focal length of 12.7 mm, a fiber bundle and a prism utilized to direct the laser pulses to the tissue surface. The diameter of the whole imaging probe is 14.7 mm. The laser spot and acoustic focus are carefully adjusted to achieve partial overlap to achieve a better SNR of PA signals. The probe is mounted on a motorized rotator to achieve sector scanning. A lifting motor is integrated with the rotator to realize scanning in Z direction with a step of $250 \mu\text{m}$. A resinous holder is designed and printed via a 3D printer to immobilize the tongue as shown in Fig. 1(b). The imaging window inside the holder is sealed with a piece of ultrathin plastic membrane. In the experiments, the volunteer would bite the resinous holder and the tongue was tightly attached to the membrane with drinkable water filling the gap. The internal space of the resinous holder was filled with water serving as the coupling medium for ultrasound transmission.

2.3. Phantom preparation

To evaluate the performance of the system, 12 human hairs with a diameter of $60 \mu\text{m}$ were located in the tissue-mimicking background perpendicularly to the imaging plane and spread away from the center with a constant increment of 0.8 mm. The background was made by the mixture of agar, deionized water, India ink and intralipid, which had an optical absorption coefficient of 0.007 mm^{-1} and a reduced optical scattering coefficient of 1.0 mm^{-1} . The imaged size of hair was used to characterize the lateral resolutions of PA and ultrasound imaging.

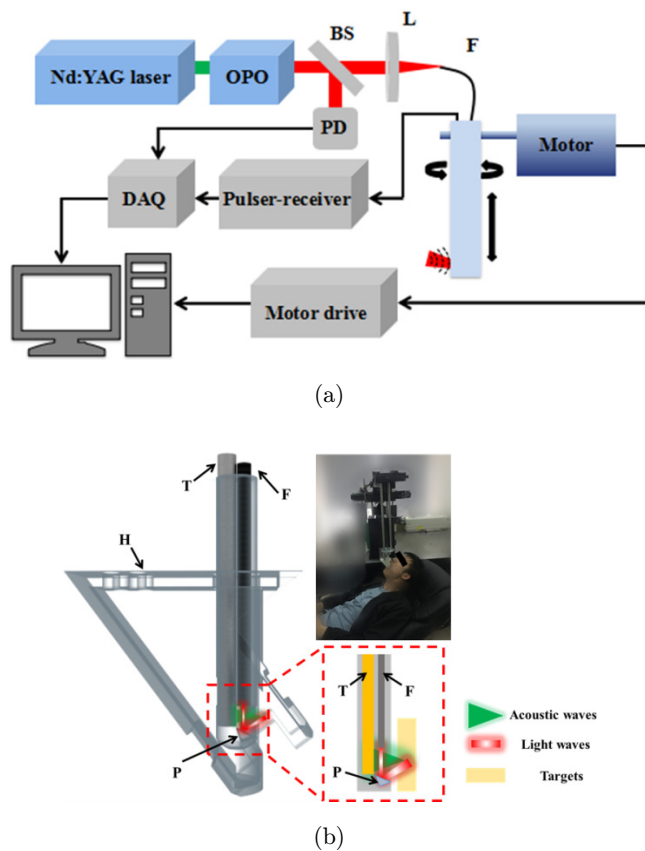


Fig. 1. (a) The schematic of the integrated system. OPO: Optical Parametric Oscillator, BS: Beam splitter, L: Convex lens, PD: Photodiode, F: Fiber, DAQ: Data acquisition system. (b) 3D rendering of the imaging interface (left), photograph of the volunteer receiving inspection (top right), and close-up view of the part indicated by the dashed rectangle in the imaging interface (bottom right). H: resinous holder, T: Transducer, F: Fiber bundle, P: Prism.

H. Guo et al.

In addition, to assess the performance of PA and ultrasound imaging on tumor detection, three groups of cylindrical tumor-mimicking targets with a diameter of 0.8 mm were prepared. The first group of targets were made of solidified agarose phantom with an optical contrast of 10 and no acoustic contrast to the tissue-mimicking background. The second group of targets were made of transparent epoxy which had the acoustic contrast of 1.5 and no optical contrast to the background. The third group of targets had both optical and acoustic contrasts of 10 and 1.5, respectively, by mixing India ink, intralipid and transparent epoxy.

2.4. Tumor model and experiments

Mouse mammary carcinoma 4T1 cells were cultured at 37°C in a humidified incubator supplemented with 10% fetal bovine serum and antibiotics. Cells were harvested at 80% confluence. 2×10^6 cells were implanted into the mammary fat pads of 6–8 week-old female BALB/C mice. Tumors were allowed to progress for 7–10 days to a size of 4 mm prior to the *in vivo* experiments. Animals were provisionally anesthetized using isoflurane with precision vaporizer at 1–1.5% followed by injection of a mixture of ketamine (85 mg/kg) and xylazine (4 mg/kg). We mounted the imaging probe on a two-dimensional stepper motor and did a dual-modality raster scan of the tumors with an interval of 0.1 mm. An entire imaging area of 10 mm \times 10 mm was covered. We imaged the tumors *in vivo* by adding additional biological tissues to the top of the mouse skin. After the experiments, all mice were sacrificed using University of Electronic Science and Technology of China (UESTC)-approved techniques.

3. Results

Figures 2(a) and 2(b) show the representative PA and ultrasonic B-scan images of hairs embedded at different depths in the background. In the experiments, each B-scan image covers a 270° field of view (FOV) formed by 360 A-lines. From both the PA and ultrasonic images, when the hairs move away from the acoustic focus indicated by the white arrows, the lateral resolution deteriorates. Based on the fundamental of acoustic-resolution PA microscopy and B-mode ultrasound imaging, the best lateral resolution is determined by the size of the acoustic focus. In the current setup, the best

theoretical lateral resolution is calculated to be 320 μm according to the center frequency, aperture size, and focal length of the transducer. We plot the lateral profiles of the hair indicated by the white arrows in Figs. 2(c) and 2(d). Full widths at half maximum (FWHMs) of the profiles are considered to be the best lateral resolutions of PA and ultrasound images, which are 420 μm and 340 μm , respectively. The results suggest that the measured lateral resolutions are slightly worse than the theoretical one. The major reasons for this discrepancy are probably that the probe may not be positioned in an absolute vertical state and the hair used to estimate the best lateral resolution is slightly off the acoustic focus. The axial resolution of the system is approximately 92 μm determined by the center frequency of the transducer.²⁷ The maximum penetration depth for human hair is measured to be more than 15 mm. As shown in Figs. 2(e) and 2(f), both photoacoustic and ultrasound signals have the best signal-to-noise ratios (SNRs) of 32 dB and 34 dB at the acoustic focus, and both SNRs deteriorate when the targets locate off the focus.

In additional phantom experiments, we scanned three groups of tissue mimicking phantoms with 160 A-lines covering the FOV of 120°. Figures 3(a) and 3(b) show the PA and ultrasound B-scans of the first phantom with PA-contrast-only targets. We find that all three targets are invisible to ultrasound imaging due to the lack of acoustic contrast. In the second phantom with acoustic-contrast-only targets, as shown in Figs. 3(c) and 3(d), all the targets are only visible to ultrasound imaging. As we expected, in the third phantom containing targets with both PA and acoustic contrast, PA and ultrasound imaging can visualize them clearly as shown in Figs. 3(e) and 3(f). These results suggest that both imaging modalities are able to detect real tumor lesions with sufficient sensitivity, and complement each other in comprehensive situations. We note that, in PA images, only boundaries of targets are clearly identified with the loss of inside information. This phenomenon is due to the high center frequency and limited response bandwidth of the transducer leading to the loss of the low-frequency PA signals.

To evaluate the clinical potential of this technique for detecting tongue cancer in human, we imaged animal tumors *in vivo* and evaluated the penetration depth by adding additional chicken breast to the top of the tumors. Figure 4(a) shows

Photoacoustic and ultrasound imaging for tongue cancer detection

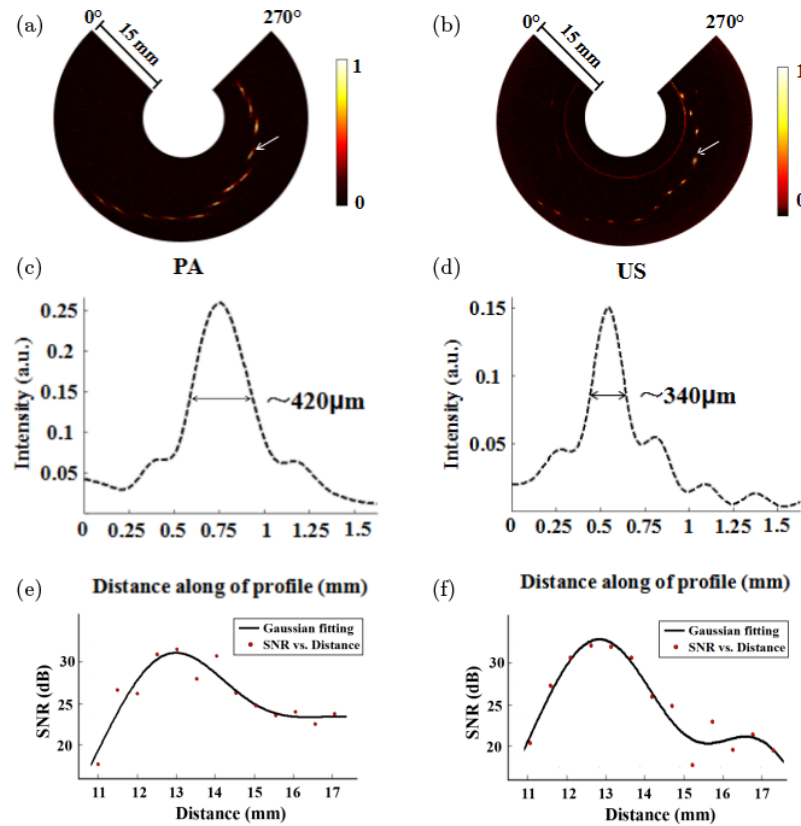


Fig. 2. Evaluation of the system resolutions and SNRs. (a) and (b) Representative PA and ultrasonic B-scan images (Hilbert transformed) acquired from the hair phantom. (c) and (d) FWHM of the profiles for the selected targets located at the acoustic focus indicated by white arrows in (a) and (b). (e) and (f) Calculated SNRs of the hair with the increase of the depth.

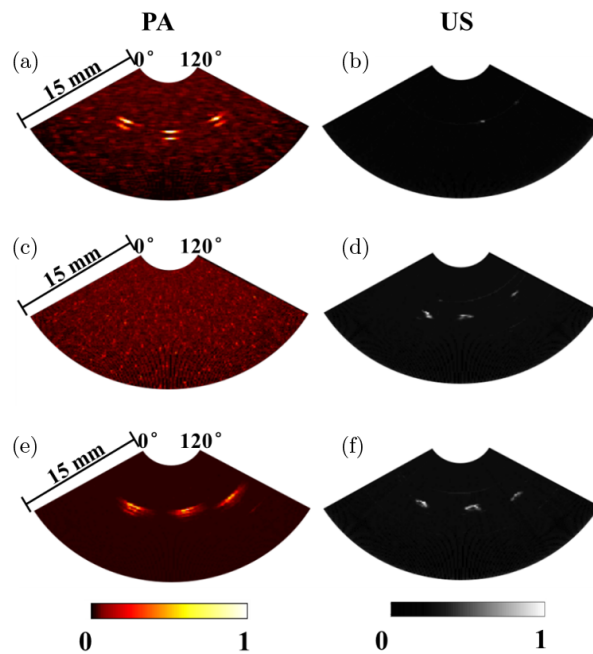


Fig. 3. PA and ultrasonic B-scan images of tissue mimicking phantoms. (a) and (b) The first group of targets with an optical contrast and no acoustic contrast. (c) and (d) The second group of targets with an acoustic contrast and no optical contrast. (e) and (f) The third group of targets with both optical and acoustic contrasts.

H. Guo et al.

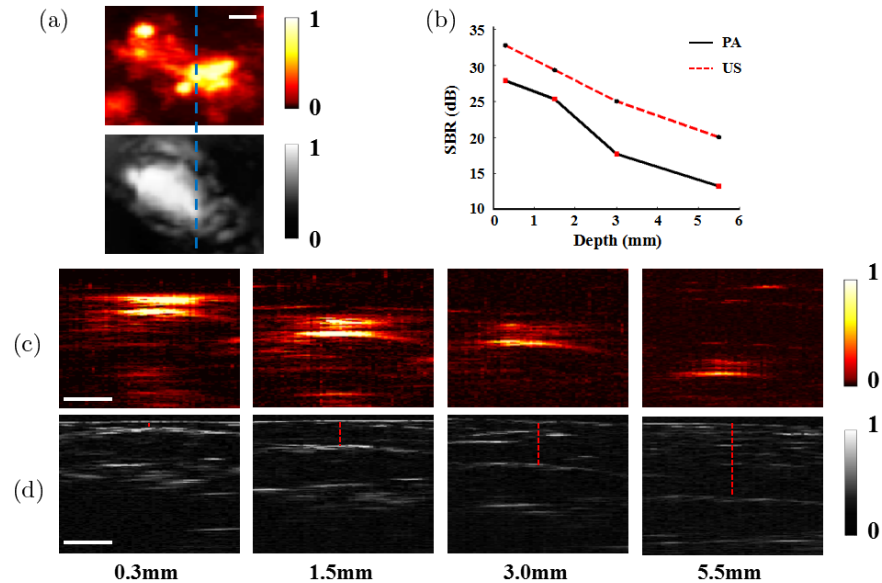


Fig. 4. Evaluation of the imaging depths and SBRs of both imaging modalities using a mouse tumor model. (a) PA (top) and ultrasonic (bottom) MAP images of a tumor without adding chicken breast. The dashed blue lines indicated the position of the selected cross-sections of PA and US. (b) SBRs vs depth. (c) and (d) PA (top row) and ultrasonic (bottom row) B-Scan images by adding different thicknesses of chicken breast, respectively (The red dashed line represents the thickness of chicken breast. 0.3, 1.5, 3.0 and 5.5 mm, respectively). Scale bar: 1 mm.

the PA and ultrasonic maximum amplitude projections (MAPs) of the tumor in a mouse without adding chicken breast, respectively. The dashed blue line represents the position of PA and ultrasonic B-scan images shown in Figs. 4(c) and 4(d). The tumors of the mice are clearly imageable even after adding 5.5-mm thickness of chicken breast. As the imaging depth increased, the signal to background ratio (SBR) decreased from 28 to 13 dB and from 32 to 20 dB as shown in Fig. 4(b), respectively.

To validate the feasibility of this probe in clinical application, normal human tongues of the healthy volunteers were imaged. We have obtained consents

from the volunteers. Figure 5 shows the PA and ultrasonic B-scan images of four typical layers. The images cover 60° FOVs corresponding to 80 A-lines. In PA images, we can clearly see many large blood vessels and clusters of small ones. In US images, the inside structure changes of tongue were clearly identified. The red dotted lines represent the surfaces of the tongue in different positions. In human cases, the penetration depth of PA and ultrasound imaging is 5.5 mm, which is sufficient to cover the thickness of human tongue under the flattened condition. We present the co-registered three-dimensional data in Medias 1 and 2.

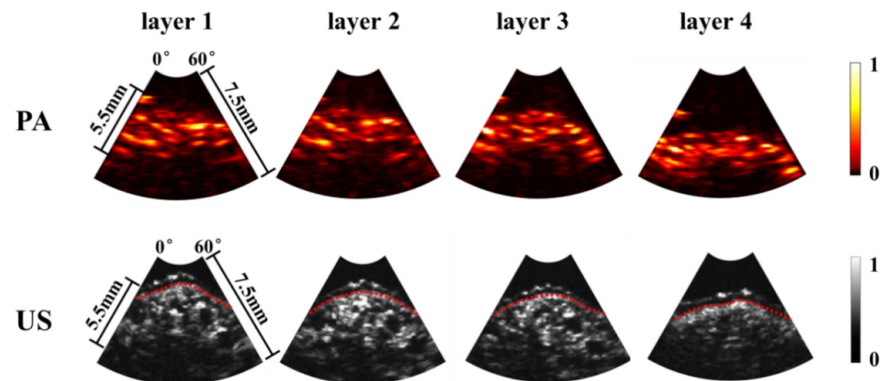


Fig. 5. *In vivo* photoacoustic (top row) and ultrasonic (bottom row) B-scan images of four typical tongue slices (~ 7.5 mm depths are displayed). In the US images, the red dashed line represents the surfaces of the tongue.

4. Discussion

In this study, we propose and design a dual-modality PA and ultrasound imaging probe, which has the potential for early-stage tongue cancer detection. The PA and ultrasound modalities yield to lateral resolutions of $420\ \mu\text{m}$ and $340\ \mu\text{m}$, respectively. The maximum penetration depth can reach up to 15 mm for imaging blood vessels and 5.5 mm for tumor lesions, which is sufficient for tongue cancer detection. Compared with previous studies, we have carried out experiments of human tongue to further assess the feasibility of this technique in clinics. The results indicate that the penetration depth of PA and ultrasound imaging is 5.5 mm which is sufficient to cover the entire tongue, PA imaging is able to detect blood vessels associated with early-stage cancerous tissue, and ultrasound imaging is capable of imaging the internal structures of the tongue. Although we have demonstrated the great potential of this system in tongue cancer detection, some challenges and several further improvements are still needed to overcome and implement this system. First, a high-frequency ultrasound transducer with a shorter focal length can significantly improve the sensitivity and spatial resolution of the imaging system. Second, a higher repetition rate laser source is needed to improve the imaging speed and promote clinical applications in tongue cancer. Third, we did a preliminary study in human which just suits for the tongue inspection. However, the internal structure of the oral cavity is much more complicated than other organs such as breast, colon, and esophagus. Therefore, it is challenging to design a universal PA imaging interface suitable for the entire oral cavity. In order to inspect the entire mouth, efforts will be focused on miniaturization and design of specific imaging interfaces for different subjects inside the oral cavity.

Acknowledgments

This work was sponsored by National Natural Science Foundation of China (81571722 and 61528401), State International Collaboration Program from Sichuan (2016HH0019), the Fundamental Research Funds for the Central Universities (ZYGX2015J146), and startup grant (A03012023601011) from University of Electronic Science and Technology of China. Heng Guo and Weizhi Qi contributed equally to this work.

References

1. D. M. Parkin, F. Bray, J. Ferlay, P. Pisani, "Global cancer statistics, 2002," *CA Cancer J. Clin.* **55**, 74–108 (2005).
2. American Cancer Society, Cancer facts and figures 2006, American Cancer Society, Atlanta (2006).
3. N. Howlader, A. M. Noone, M. Krapcho, N. Neyman, R. Aminou, S. F. Altekruse, C. L. Kosary, J. Ruhl, Z. Tatalovich, H. Cho, A. Mariotto, M. P. Eisner, D. R. Lewis, H. S. Chen, E. J. Feuer, K. A. Cronin, SEER Cancer Statistics Review, 1975-2009 (Vintage 2009 Populations), National Cancer Institute (2012).
4. C. Scully, J. V. Bagan, C. Hopper, J. B. Epstein, "Oral cancer: Current and future diagnostic techniques," *Am. J. Dent.* **21**, 199–209 (2008).
5. J. H. Takano, T. Yakushiji, I. Kamiyama, T. Nomura, A. Katakura, N. Takano, T. Shibahara, "Detecting early oral cancer: Narrowband imaging system observation of the oral mucosa microvasculature," *Int. J. Oral Maxillofac. Surg.* **39**, 208–213 (2010).
6. M. Muto, C. Katada, Y. Sano, S. Yoshida, "Narrow band imaging: A new diagnostic approach to visualize angiogenesis in superficial neoplasia," *Clin. Gastroenterol. Hepatol.* **3**, 16–20 (2005).
7. A. Gillenwater, R. Jacob, R. Ganeshappa, B. Kemp, A. K. El-Naggar, J. L. Palmer, G. Clayman, M. F. Mitchell, R. Richards-Kortum, "Noninvasive diagnosis of oral neoplasia based on fluorescence spectroscopy and native tissue autofluorescence," *Arch. Otolaryngol. Head Neck Surg.* **124**, 1251–1258 (1998).
8. D. L. Heintzelman, U. Utzinger, H. Fuchs, A. Zuluaga, K. Gossage, A. M. Gillenwater, R. Jacob, B. Kemp, R. R. Richards-Kortum, "Optimal excitation wavelengths for in vivo detection of oral neoplasia using fluorescence spectroscopy," *Photochem. Photobiol.* **72**, 103–113 (2000).
9. C. S. Kim, P. Wilder-Smith, Y. C. Ahn, L. H. L. Liaw, Z. Chen, Y. J. Kwon, "Enhanced detection of early-stage oral cancer in vivo by optical coherence tomography using multimodal delivery of gold nanoparticles," *J. Biomed. Opt.* **14**, 034008 (2009).
10. M. T. Tsai, H. C. Lee, C. K. Lee, C. H. Yu, H. M. Chen, C. P. Chiang, C. C. Chang, Y. M. Wang, C. C. Yang, "Effective indicators for diagnosis of oral cancer using optical coherence tomography," *Opt. Express.* **16**, 15847–15862 (2008).
11. J. Furusawa, N. Oridate, F. Suzuki, A. Homma, Y. Fureta, S. Fukuda, "Initial CT findings in early tongue and oral floor cancer as predictors of neck metastasis," *Oral Oncol.* **44**, 793–797 (2008).
12. T. T. A. Peters, J. A. Castelijns, R. Ljumanovic, B. I. Witte, C. R. Leemans, R. Bree, "Diagnostic

H. Guo et al.

- value of CT and MRI in the detection of paratracheal lymph node metastasis," *Oral Oncol.* **48**, 450–455 (2012).
13. P. Lam, K. M. Au-Yeung, P. W. Cheng, W. I. Wei, A. P. Yuen, N. Trendell-Smith, J. H. Li, R. Li, "Correlating MRI and histologic tumor thickness in the assessment of oral tongue cancer," *AJR.* **182**, 803–808 (2004).
 14. R. Sigal, A. M. Zagdanki, G. Schwaab, J. Bosq, A. Auperin, A. Laplanche, J. P. Francke, F. Eschwege, B. Luboinski, D. Vanel. "CT and MRI imaging squamous cell carcinoma of the tongue and floor of the mouth," *Radiographic* **16**, 787–810 (1996).
 15. L. V. Wang, S. Hu, "Photoacoustic tomography: in vivo imaging from organelles to organs," *Science* **335**, 1458–1462 (2012).
 16. P. Beard, "Biomedical photoacoustic imaging," *Interface Focus* **1**, 602–631 (2011).
 17. L. Xi, S. Grobmyer, L. Wu, R. Chen, G. Zhou, L. G. Gutwein, J. Sun, W. Liao, Q. Zhou, H. Xie, H. Jiang, "Evaluation of breast tumor margins in vivo with intraoperative photoacoustic imaging," *Opt. Express* **20**, 8726–8731 (2012).
 18. L. Xi, H. Jiang, "High resolution three-dimensional photoacoustic imaging of human finger joints in vivo," *Appl. Phys. Lett.* **107**, 063701 (2015).
 19. R. Kruger, C. Kuzmiak, R. Lam, D. Reinecke, S. Del Rio, D. Steed, "Dedicated 3D photoacoustic breast imaging," *Med. Phys.* **40**, 113301 (2013).
 20. D. Razansky, M. Distel, C. Vinegoni, R. Ma, N. Perrimon, R. W. Köster, V. Ntziachristos, "Multispectral opto-acoustic tomography of deep-seated fluorescent proteins in vivo," *Nat. Photonics.* **3**, 412 (2009).
 21. B. Wang, A. Karpiouk, D. Yeager, J. Amirian, S. Litovsky, R. Smalling, S. Emelianov, "Intravascular photoacoustic imaging of lipid in atherosclerotic plaques in the presence of luminal blood," *Opt. Lett.* **37**, 1244–1246 (2012).
 22. J. Yang, C. Favazza, R. Chen, J. Yao, X. Cai, K. Maslov, Q. Zhou, K. K. Shung, L. V. Wang, "Simultaneous functional photoacoustic and ultrasonic endoscopy of internal organs *in vivo*," *Nat. Med.* **18**, 1297–1302 (2012).
 23. X. Dai, L. Xi, C. Duan, H. Yang, H. Xie, H. Jiang, "Miniature probe integrating optical-resolution photoacoustic microscopy, optical coherence tomography, and ultrasound imaging: Proof-of-concept," *Opt. Lett.* **40**, 2921–2924 (2015).
 24. Y. Lao, D. Xing, S. Yang, L. Xiang, "Noninvasive photoacoustic imaging of the developing vasculature during early tumor growth," *Phys. Med. Biol.* **53**, 4203–4212 (2008).
 25. A. A. Oraevsky, A. A. Karabutov, E. B. Savateeva, B. Bell, M. Motamedi, S. L. Thomsen, P. J. Pasricha, "Opto-acoustic imaging of oral cancer: Feasibility studies in hamster model of squamous cell carcinoma," *Proc. SPIE* **3597**, 385–396 (1999).
 26. H. Fatakdawala, S. Poti, F. Zhou, Y. Sun, J. Bec, J. Liu, D. R. Yankelevich, S. P. Tinling, R. F. Gandour-Edwards, D. Gregory Farwell, L. Marcu, "Multimodal in vivo imaging of oral cancer using fluorescence lifetime, photoacoustic and ultrasound techniques," *Biomed. Opt. Express* **4**, 1724–1741 (2013).
 27. S. P. Mattison, R. L. Shelton, R. T. Maxson, B. E. Applegate, "Continuous real-time photoacoustic demodulation via field programmable gate array for dynamic imaging of zebrafish cardiac cycle," *Biomed. Opt. Express* **4**, 1451–1463 (2013).